aerospace

MDPI

Article

Design of Lattice-Based Energy-Absorbing Structure for Enhancing the Crashworthiness of Advanced Air Mobility

Jaryong Cho, Eun Suk Lee, Jeong Ho Kim, Chang-Yull Lee and Jin Yeon Cho *

Program in Aerospace Systems Convergence, Department of Aerospace Engineering, Inha University, Incheon 22212, Republic of Korea; wkfyd94@inha.edu (J.C.); eunsuk@inha.edu (E.S.L.); jeonghokim@inha.ac.kr (J.H.K.); cylee@inha.ac.kr (C.-Y.L.)
* Correspondence: cjy@inha.ac.kr

Abstract: The development of advanced air mobility—an eco-friendly, next-generation transportation system—is underway and garners significant attention. Due to the novel propulsion concept of eVTOL (electric Vertical Take-Off and Landing) and its operation in low altitude, urban environment, regulations for commercialization have not yet been established. Consequently, related research on passenger safety in emergency landings is ongoing, and this study focuses on enhancing the crashworthiness of advanced air mobility. To ensure the crashworthiness of advanced air mobility, civil airworthiness standards were referenced to determine the appropriate test conditions, and a design criterion for developing an energy-absorbing structure was derived. In this study, lattice structures are considered for designing an energy-absorbing structure that satisfies the design criterion, and finite element analysis is conducted to predict the performance of lattice structures. Based on the predicted data, surrogate models are constructed using the Kriging method according to the type of lattice structure. To verify the data obtained from numerical models, representative structures are manufactured using EBM (Electron Beam Melting) technology, and compressive tests are conducted to obtain the force–displacement curves. The test data are compared with the numerical data, and it is confirmed that the test data show good agreement with the numerical data. After this confirmation, the constructed surrogate models are utilized to select a lattice-based energy-absorbing structure that satisfies the crashworthiness-related design criterion. Finally, a crash simulation of a vertical drop test is carried out using the selected lattice structure, and results indicate that the resulting acceleration due to the collision is below the human tolerance limit, thereby verifying the crashworthiness of the energy-absorbing structure.

Keywords: lattice structure; energy-absorbing structure; mean crushing force; advanced air mobility; surrogate model; metal additive manufacturing

check for updates

Academic Editor: Sebastian Heimbs

Received: 4 March 2025
Revised: 31 March 2025
Accepted: 10 April 2025
Published: 12 April 2025

Citation: Cho, J.; Lee, E.S.; Kim, J.H.; Lee, C.-Y.; Cho, J.Y. Design of Lattice-Based Energy-Absorbing Structure for Enhancing the Crashworthiness of Advanced Air Mobility. *Aerospace* **2025**, *12*, 332. https://doi.org/10.3390/aerospace12040332

Copyright: © 2025 by the authors. Licensee MDPI, Basel, Switzerland. This article is an open access article distributed under the terms and conditions of the Creative Commons Attribution (CC BY) license (https://creativecommons.org/licenses/by/4.0/).

1. Introduction

AAM (Advanced Air Mobility) has the potential to transform urban and regional transportation by providing efficient and innovative mobility solutions [1]. While technological advancements such as propulsion systems, aerodynamics, and noise reduction in eVTOL vehicles have been the focus of extensive research [2], passenger safety in emergency situations, such as crashes or emergency landings, remains underexplored. This deficiency directly affects passenger safety and reduces public acceptance of AAM [3]. Considering AAM's unique operational conditions, such as low altitudes and urban environments, it is required to re-investigate conventional crashworthiness assessment strategies [4].

Crashworthiness is defined as "the ability of an aircraft, its systems, and components to protect occupants during a crash" [5]. Current U.S. Federal Aviation Regulations for crashworthiness are developed based on the USARTL-TR-79-22B document, which analyzed survivable crash conditions for rotary-wing aircraft between 1971 and 1976 [6]. These standards aim to ensure high survival rates during emergency landings. This study builds guidelines such as EASA (European Union Aviation Safety Agency) and FAA (Federal Aviation Administration) regulations to analyze energy-absorbing structures, which are designed to limit the acceleration transmitted to passengers during ground collisions [7–9]. Especially in this paper, FAA regulations were mainly referenced among other regulations, such as ICAO (International Civil Aviation Organization) standards, due to their detailed and stringent crashworthiness requirements. As the main regulatory body for U.S. civil aviation, the FAA developed FARs, which provide comprehensive guidelines on structural integrity and crashworthiness. These regulations are globally recognized for their technical depth and are commonly referenced in crashworthiness research.

Energy-absorbing systems are crucial for AAM, as they mitigate the loads experienced by the fuselage and passengers during emergency scenarios. Examples of energy-absorbing systems include vehicle bumpers, crumple zone structures, energy-absorbing honeycomb structures, and similar designs. Such systems have broad applications across industries, and ongoing research aims to improve their performance for various cases [10,11]. If the structure is overly rigid, it may not absorb energy effectively, which can result in an excessive transfer of energy to the passengers. In line with this reasoning, this study first derives a design criterion that suggests an acceptable range for the *MCF* (Mean Crushing Force) of the energy-absorbing structure based on the collision speed of AAM in emergency landing conditions and the total mass of AAM to meet the safety requirements.

In this work, a lattice-based structure is adopted as an energy-absorbing structure, considering its potential [12]. Lattice structures consist of repetitive unit cells that strongly influence the macroscopic behavior of the entire structure. Lattice structures provide an excellent balance of strength and lightweight properties, making them ideal for applications where weight reduction is critical. Their strength-to-weight efficiency makes them valuable for aerospace engineering solutions. In this study, the BCCz+cross structure is considered for the unit cell of the lattice structure due to its superior energy-absorbing performance [13]. The BCCz+cross unit cell comprises a BCC (Body-Centered Cubic) unit cell with vertical and X-shaped cross-linked auxiliary struts. As mentioned before, the macroscopic behavior of the lattice structure is strongly dependent on the unit cell. Based on this observation, some studies have been conducted in the past to improve energy absorption performance.

Maskery et al. [14] sought to enhance the energy absorption performance of the lattice structure by controlling a density gradient along one direction. The density gradient was manipulated by altering the strut thickness. Their work showed that increasing the strut thickness in the compression direction caused the compressive crushing force to increase gradually with compression, which is unfavorable from the energy absorption standpoint. From the energy absorption perspective, it is preferable to maintain a compressive crushing force that remains constant regardless of compression displacement. Mostafa et al. also aimed to enhance the mechanical performance of lattice structures by changing the unit cell size and density in each location of the lattice structure [15]. Their approach has a general aspect. However, unfortunately, it is difficult to maintain the total mass of the lattice structure within their framework, even though the mass budget is one of the most important factors in the actual design procedure for AAM.

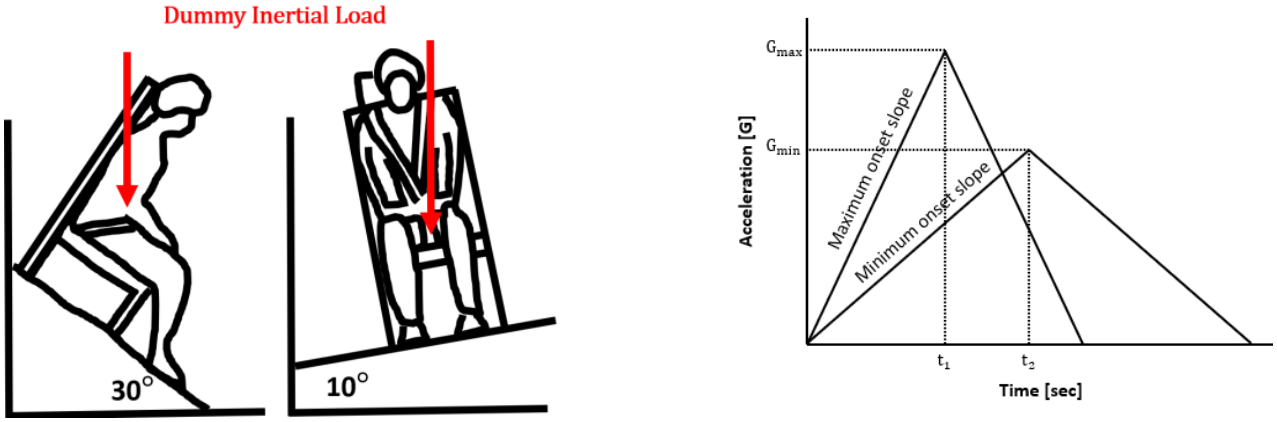
To avoid these drawbacks in previous works [14,15], this study adopts a specific group-wise density control scheme where the unit cells are grouped, and the thickness of the struts in each unit cell group is changed while maintaining the total mass unchanged. This

approach makes it possible to quantitatively compare various lattice structures under the same constant mass condition. To evaluate the energy absorption performance, quasi-static compression analysis is carried out using the FE (finite element) method [16]. For FE analysis, the commercial software ABAQUS Explicit 2024 is utilized. Using the universal Kriging method along with the finite element analysis data, a response surface model is constructed to adopt the appropriate lattice structure design for AAM [17–19]. To verify the energy-absorbing performance of the currently designed structure, a lattice structure with adjusted internal density is designed using a CAD (Computer Aided Design) program and manufactured via EBM (Electron Beam Melting), a metal additive manufacturing technology. The lattice structure is manufactured using Ti-6Al-4V, a material extensively used in aerospace applications due to its high specific strength and excellent corrosion resistance [20]. A quasi-static compression test is performed using a UTM (Universal Test Machine), and the experimental results are compared with the simulation data to validate the energy absorption performance [21]. As a final example, a crash simulation of a vertical drop test of the lattice structure, designed using the proposed approach, is performed to evaluate the usefulness and applicability of the proposed design methodology. Through the proposed design methodology for 3D-printed energy-absorbing lattice structures, this work aims to ensure passenger safety during emergency landings of AAM vehicles, thereby enhancing their social acceptance.

2. Methodology

2.1. Crashworthiness of Advanced Air Mobility

Various documents outline test conditions and regulations for evaluating crashworthiness, including emergency landing conditions and human acceleration limits. Among these, the technical document USARTL-TR-79-22B presents dynamic testing methodologies based on accident case studies of light rotary-wing aircraft. The specifications presented in the document are illustrated in Figure 1 and correspond to the conditions in Table 1. In Table 1, t_2 refers to a rise time and G_{min} refers to the deceleration measured near the seat position. The dynamic test conditions for light rotary-wing and fixed-wing aircraft are also outlined in MIL-STD-1290A and AS8049B [22].



(**a**) Dynamic test configuration (**b**) Dynamic test acceleration during time

Figure 1. Dynamic test requirements for qualifications and for research/development testing—USATRL-TR-79-22A [5].

For AAM vehicles, the regulations on dynamic test conditions have not yet been provided, even by the FAA. However, dynamic test conditions for newly designed aircraft are usually based on previous dynamic conditions. Therefore, in this study, the emergency landing test conditions in U.S. Federal Aviation Regulations part 23/27 in Table 2 are

referenced for AAM to verify the suitability of energy-absorbing structures. The test conditions of this study are based on the fuselage emergency landing dynamic tests of light fixed-wing and light rotary-wing aircraft in conservative situations. The test conditions of the full-scale eVTOL crash test conducted by NASA (National Aeronautics and Space Administration) are also referenced [23]. Considering the aforementioned test conditions, this study takes a conservative approach and adopts the vertical drop velocity of 10 m/s, which corresponds to 32.8 ft/s.

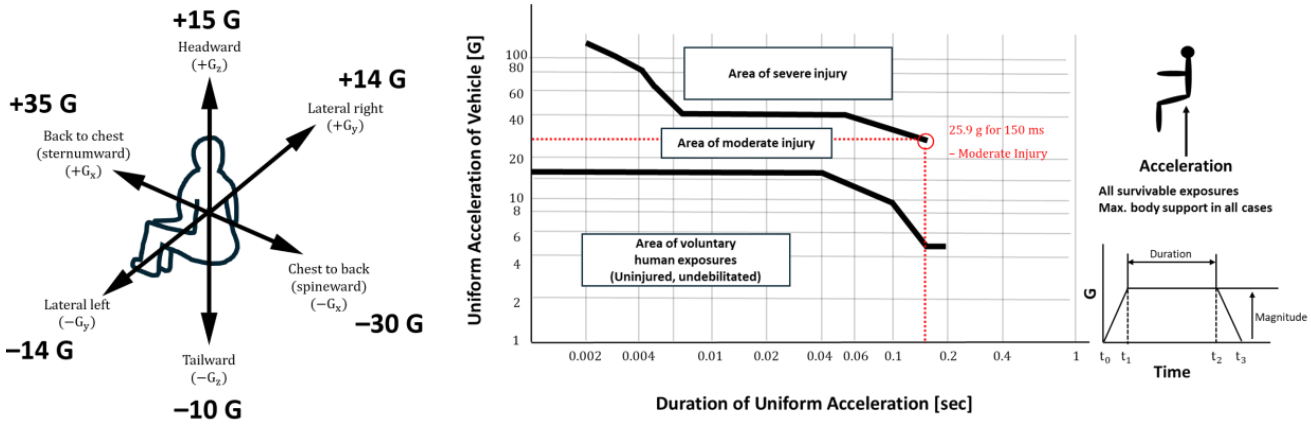
Table 1. Dynamic test requirements for helicopter seat—AS8049B [22].

Dynamic Test Conditions for Cockpit Seats	
Minimum Velocity [m/s]	9.14
Maximum t_2 [s]	0.031
G_{min} [G]	30

Table 2. Conditions for vertical drop test of Advanced Air Mobility [8,9,23].

Horizontal–Vertical Drop Test Condition	Part 23.562 -Utility Airplane	Part 27.562 -Normal Rotorcraft	NASA eVTOL Crash Test
Test velocity [ft/s]	31	30	31.4
Seat Pitch Angle [°]	60	60	.
Seat Yaw Angle [°]	0	0	.
Minimum Acceleration [G]	19/15	30	.
Time to Peak [s]	0.05/0.06	0.031	.
Floor Deformation [°]	None	10 Pitch/10 Roll	.

Under emergency landing conditions, final safety is ensured by verifying that the acceleration experienced by the human body remains within the human tolerance limits. To determine human tolerance, the Eiband curve in Figure 2 can be used. The Eiband curve, specified in USARTL-TR-79-22A, was established in 1959 as a result of numerous acceleration tests and studies conducted to determine the human response to crashworthiness.



(**a**) (**b**)

Figure 2. Configuration of human tolerance. (**a**) Terminology for directions of forces on the body. (**b**) Duration and magnitude of Headward acceleration Eiband Curve [5].

Human Tolerance in the vertical direction (Headward) was initially 18 G and is now commonly recognized as 15 G, as shown in Figure 2a. However, this does not necessarily

mean that the acceleration on the human body should not exceed 15 G, and the concept of acceleration duration should be added. The impact of acceleration and duration on human safety can be analyzed using the Eiband curve, as shown in Figure 2b. For example, even if an acceleration of 25.9 G on headward direction lasts for 150 ms, it is classified as a moderate injury level according to the Eiband curve. In this study, a conservative vertical drop impact velocity of 10 m/s is assumed, and a target acceleration of 20 G in the headward direction is selected to ensure that the acceleration under emergency landing conditions does not exceed 25.9 G, which is considered a moderate injury level. Human safety can be validated by ensuring that the acceleration at which the energy-absorbing device operates does not exceed a specific threshold. By calculating vertical acceleration, it can be demonstrated that if it does not exceed 25.9 G, the crashworthiness of the aircraft can be satisfied [24].

2.2. Energy-Absorbing Structure

In this study, lattice structures are adopted as the energy-absorbing structure. These structures consist of repetitive unit cells, the type of which is crucial in determining the mechanical behavior of the lattice structure. Each unit cell comprises interconnected struts that, depending on their internal arrangement, provide structural robustness despite their low mass. This makes lattice structures promising for use in various industries such as aviation, marine, and construction [25]. In this study, the BCCz+cross unit cell structure, as shown in Figure 3, incorporating vertical and X-shaped cross-linked horizontal auxiliary struts into a BCC design, is selected for its improved energy-absorbing capability compared to the BCC unit cell structure, as reported in reference [13].



(**a**) Unit cell of BCC structure (**b**) Unit cell of BCCz+cross structure

Figure 3. Design of BCCz+cross structure based on the BCC structure.

2.3. Requirements for Energy Absorber

To quantitatively understand and compare the energy-absorbing performance of the structures designed in this study, energy absorption indicators are introduced in this study. These indicators can be summarized as follows [26,27]:

2.3.1. Energy Absorption, EA

EA is the total amount of energy absorbed by the structure as it undergoes plastic deformation during compression. It is calculated by integrating the crushing force F over the displacement from the initial displacement d_i, where compression starts, to the final displacement d_f, where the point compressive force instantly goes up since the structure is overly compressed and densified. EA is the energy that the structure can absorb in the event of an impact, providing an indication of sufficient energy absorption. In general, the

force–displacement curve for a structure subjected to compressive deformation looks like Figure 4, where the area of the graph represents the EA, which is equal to Equation (1).

$$EA = \int_{d_i}^{d_f} F dx \tag{1}$$

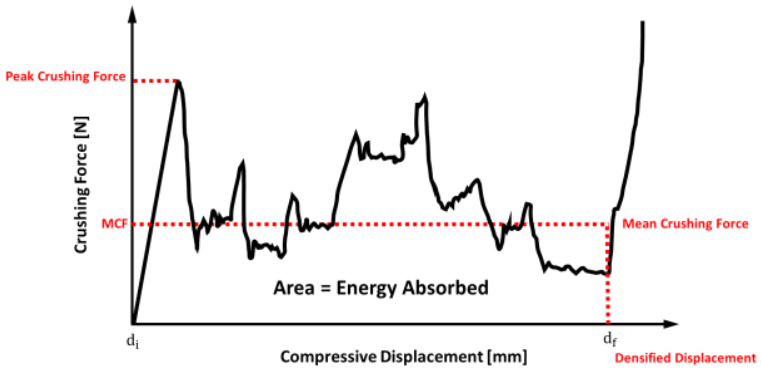


Figure 4. Typical force–displacement curve of energy-absorbing structure.

2.3.2. Mean Crushing Force, *MCF*

MCF is the Mean Crushing Force, which refers to the average compressive force applied during the deformation of the structure. Generally, it is the total absorbed energy divided by the compressive displacement up to the point of densification, as given by Equation (2).

$$MCF = \frac{1}{d_f - d_i} \int_{d_i}^{d_f} F dx \tag{2}$$

In this study, *MCF* is considered the most important performance indicator for the energy-absorbing structure. Generally, during an impact, an associated impact force exists. If the *MCF* of the energy-absorbing structure is too high compared to the impact force, the structure does not collapse sufficiently, resulting in insufficient absorption of kinetic energy and high acceleration transmission. Conversely, if the *MCF* of the energy-absorbing structure is too low compared to the impact force, the structure will entirely collapse before absorbing the total kinetic energy, causing the residual kinetic energy to result in potentially fatal acceleration.

Therefore, the *MCF* of energy-absorbing structures should be within a specific range to adequately absorb the collision energy. In Figure 5, this specific range of *MCF* is presented conceptually. *MCF* can be used as an indicator to assess the applicability of energy-absorbing structures during emergency landings.

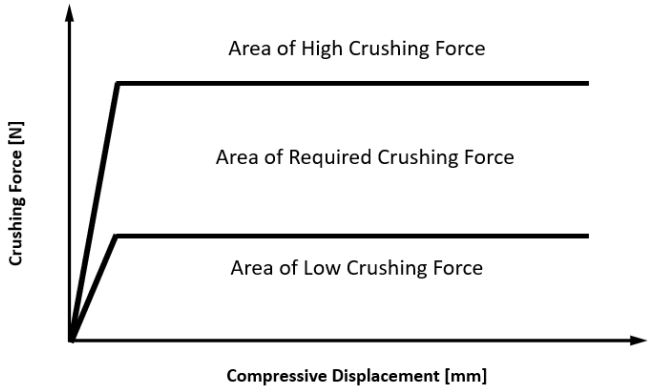


Figure 5. Required *MCF* range of energy-absorbing structure.

In the following, the specific range for *MCF* is derived to satisfy the crashworthiness design requirements. First, the crushing force is assumed to be *MCF*, although it changes during the vertical drop collision event. Additionally, it is assumed that the mass of the energy-absorbing structure is negligible compared to the total mass of the AAM for simplicity. Then, during the vertical drop situation, the equation of motion of AAM is written as follows.

$$Ma = Mg - F \tag{3}$$

where M and a denote the total mass of AAM and its acceleration, respectively. The gravitational acceleration and *MCF* are denoted by g and F, respectively. The initial conditions are the velocity and displacement just before the collision. Therefore, the collision velocity of AAM is used as the initial velocity v_0. Similarly, the initial displacement u_0 can be selected as '0' if we select the reference frame just before the collision. In this definition, the displacement becomes equal to the deformed length of the energy-absorbing structure.

Meanwhile, acceleration a and velocity v satisfy the following relationship.

$$\int_{v(0)}^{v(t_f)} v dv = \int_{u(0)}^{u(t_f)} a du \tag{4}$$

where u denote the displacement. The final time t_f refers to the time when the collision ends and AAM comes to a stop. Thus, it means that the final velocity of AAM $v(t_f)$ is 0 m/s. Since the applied forces are assumed to be constant during the collision event, acceleration is constant. Therefore, the integration of Equation (4) becomes Equation (5), noting that $u(0)$ and $v(t_f)$ are '0'.

$$a = -\frac{{v_0}^2}{2u(t_f)} \tag{5}$$

On the other hand, we have to design the crushable length of the energy-absorbing lattice structure sufficiently longer than the maximum deformed length. Therefore, the crushable length of the energy-absorbing lattice structure satisfies the following relationship (6).

$$\left|u(t_f)\right| = \left|\frac{-{v_0}^2}{2a}\right| \leq L_{crush} \tag{6}$$

where L_{crush} denotes the crushable length of the energy-absorbing lattice structure. Noting that the acceleration should be less than the survivable acceleration limit $a_{\max}$, the relationship (6) can be written as follows.

$$\frac{{v_0}^2}{2L_{crush}} \leq |a| \leq a_{\max} \tag{7}$$

Since a is negative in deceleration, inequality condition (7) can be rewritten as follows using Equation (3).

$$\left(\frac{{v_0}^2}{2L_{crush}} + g\right) \leq \frac{F}{M} \leq (a_{\max} + g) \tag{8}$$

This design criterion (8) indicates an acceptable range for the Mean Crushing Force F (*MCF*) of the energy-absorbing structure based on the emergency landing speed v_0 and mass M of AAM to meet the safety requirements.

Additionally, one can obtain the constraint equation for the crushable length of the energy-absorbing lattice structure L_{crush} from Equation (7) as follows.

$$\frac{{v_0}^2}{2a_{\max}} \leq L_{crush} \tag{9}$$

For a given mass M of AAM and the emergency landing speed v_0, the adjustable parameter in the design criterion (8) is the crushable length L_{crush} of the energy absorption structure. By increasing L_{crush}, it allows us to use energy-absorbing structures with lower crushing force. However, since the human tolerance limit is a fixed parameter, the upper limit for the crushing force of the energy-absorbing structure cannot be changed.

2.4. Design of Energy-Absorbing Structure

Generally, for lattice structure-based energy absorption structures, as the thickness of the unit struts increases, the mass increases, and the compressive force also increases. The BCCz+cross structure used in this study is an enhanced model derived from the BCC structure by incorporating the vertical and X-shaped cross-linked horizontal auxiliary struts. Among the strut components, the vertical strut influences structural buckling during compression failure, as shown in Figure 6. As the strut radius increases, the critical buckling load of the vertical strut increases, leading to an overall increase in the compressive load. On the other hand, as the length of the strut increases, the critical buckling load decreases, resulting in a decrease in the compressive load [28]. In this study, using the commercial CAD program CATIA, unit structures with an edge length of 12 mm are designed by increasing the radius from 0.3 mm to 1.5 mm, and their mass is calculated by CATIA.

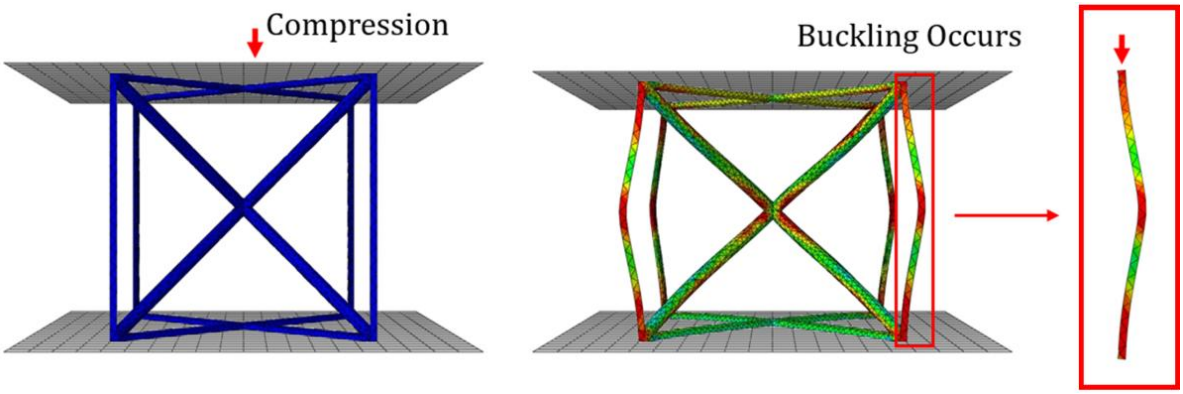


Figure 6. Buckling mode of Z strut in BCCz+cross unit cell structure in compressive analysis.

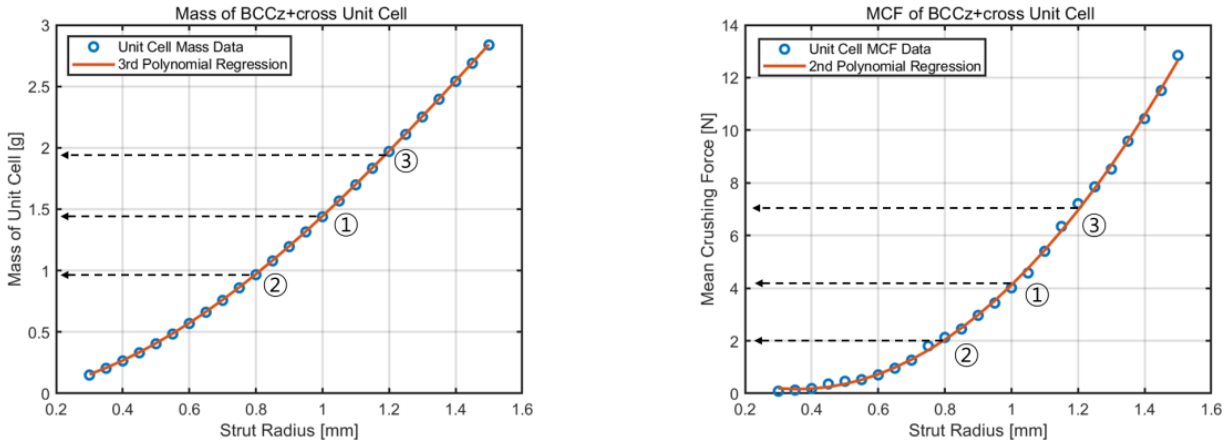
The mass of the unit structures increased according to strut radius, as shown in Figure 7a, and this is approximated using 3rd polynomial regression, as represented by Equation (10) [29]. Although the volume of a strut is proportional to the square of its radius, the regression is performed using a third-degree polynomial due to the corner geometry where the struts intersect with each other.

$$Mass = -0.35 \times r^3 + 1.78 \times r^2 + 0.02 \times r \tag{10}$$

For the designed unit cell structures, quasi-static compression analyses are carried out repetitively according to the radius thickness using the commercial finite element analysis program Abaqus 2024 [30,31], and MCF is obtained for various radius thicknesses. As the thickness increases, MCF also increases as shown in Figure 7b. Similarly to the mass, it is approximated using 2nd-order polynomial regression, as represented by Equation (11).

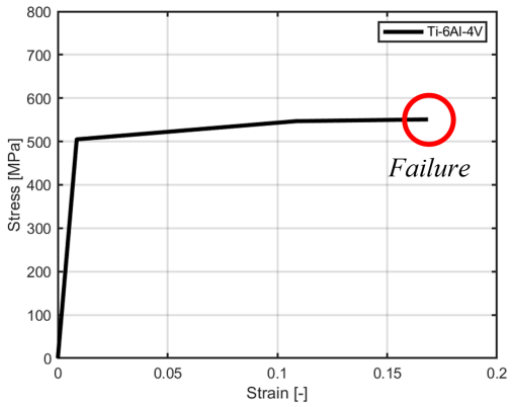
$$MCF = 9.56 \times r^2 - 6.82 \times r + 1.38 \tag{11}$$

In the finite element simulation, the unit cell structure, composed of Ti-6Al-4V, is assumed to exhibit elastoplastic behavior with isotropic hardening, and its mechanical properties are presented in Figure 8 along with the stress–strain curve.



(**a**) Mass of BCCz+cross structure (**b**) *MCF* of BCCz+cross structure

Figure 7. Polynomial regression data of mass and *MCF* changes over strut radius from 0.3 mm to 1.5 mm.



Elastic	E (MPa)	ν
-	58472	0.33
Plastic	Yield strength (MPa)	Plastic strain
(1)	505	0
(2)	548	0.1
(3)	551	0.16

Figure 8. Stress–strain curve and mechanical properties of Ti-6Al-4V.

Fixed boundary conditions are enforced on the bottom surface, while moving boundary conditions are applied to the top surface. The top surface moves downward at a uniform speed of 12 mm/s, as illustrated in Figure 9. In the finite element simulation, the C3D4 element is utilized. The model consists of 20,438 elements and 6950 nodes for the structure with a strut radius of 0.3 mm and 40,702 elements and 25,578 nodes for the structure with a strut radius of 1.5 mm. During the simulation, friction conditions are applied to the contact surfaces between the structures and the plates, with a "Hard" contact condition in the vertical direction and a friction coefficient of 0.3 in the horizontal direction.

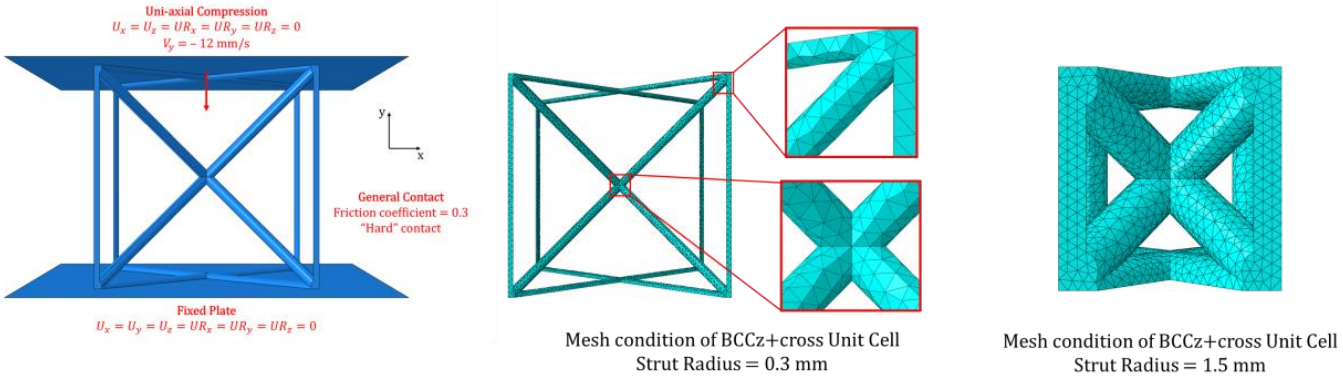
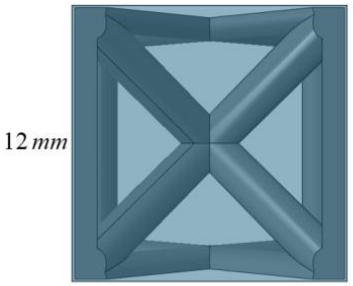


Figure 9. Finite element analysis conditions for BCCz+cross unit cell in compression test.

Through Equations (10) and (11), the mass and *MCF* of a unit cell according to the strut radius can be obtained. Let us assume there are two unit cell structures with a strut radius of 1 mm, and they are combined in parallel. Then *MCF* of a parallel combination of two unit cell structures becomes approximately twice that of a single unit cell structure. Now, let us assume that, in Figure 7a, the radius of one unit cell is reduced from ① to ② and the radius of the other unit cell is increased from ① to ③, while maintaining the total mass constant. Let us also assume that the radius of the strut for structure ① is 1 mm, while the radius of the reduced structure ② is 0.8 mm. In this phase, $Mass_i$ refers to the mass of structure ①, and MCF_i refers to the MCF of structure ①. According to Equation (10), the mass of the unit structures is calculated as $Mass_1$ = 1.45 g and $Mass_2$ = 0.98 g, respectively. The mean compressive forces are determined using Equation (11) as MCF_1 = 4.12 N and MCF_2 = 2.04 N. Given that the total mass of the structures remains constant, the combined mass of two ① structures must equal the total mass of structures ② and ③. Thus, to satisfy $Mass_3$ = 1.92 g, the radius of ③ is determined to be 1.18 mm, with the corresponding MCF_3 = 6.64 N. When the strut radius of the unit structures is identical, the total *MCF* becomes $2 \times MCF_1$ = 8.24 N, whereas when the strut radius of each cell is controlled, the total *MCF* becomes $MCF_2 + MCF_3$ = 8.68 N. From this investigation, it is noticed that the total the *MCF* of a lattice structure, composed of many unit cell structures, can be increased by controlling each unit cell mass (i.e., unit cell strut radius) while keeping the total mass constant.

In this work, lattice structures with 12 mm cube cells are considered, and the mass ratio is defined as the ratio of the volume or mass to a cube with each side measuring 12 mm. Figure 10 presents the method for calculating this ratio.

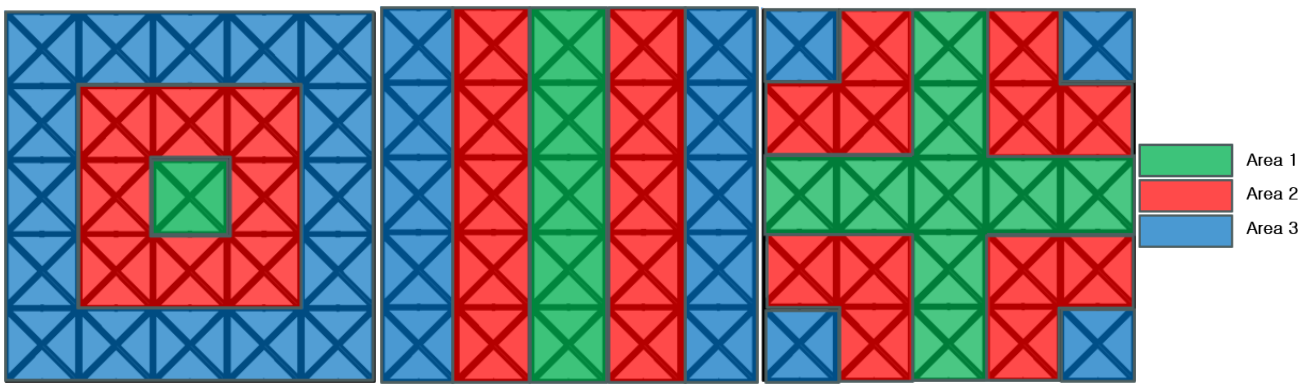


$$Volume\ of\ Cubic = 12\,mm \times 12\,mm \times 12\,mm = 1728 mm^3$$
$$Volume\ of\ BCCz + cross\ Unit\ Structure = 446 mm^3$$
$$Volume\ Ratio = Mass\ Ratio = \frac{Volume\ of\ BCCz + cross\ Unit\ Structure}{Volume\ of\ Cubic} = \frac{446}{1728} = 0.258$$

Figure 10. Calculation of mass ratio of BCCz+cross unit structure.

Through prior work, it has been known that a lattice structure with an impact surface of 5×5 cube cells gives an acceptable range of *MCF* to absorb the considered kinetic energy. Therefore, a $5 \times 5 \times 5$ lattice structure is considered to investigate the influence of density control on the crushing force. Additionally, the range of strut radius from 0.3 mm to 1.5 mm is considered, considering manufacturability and energy absorption capability.

The thickening shape type of the innermost struts is classified into three types: Center (only the central row is thickened), I (five rows are thickened in a straight shape), and Plus (nine rows are thickened in a cross shape). The shape types of thickening innermost struts are shown in Figure 11. Additionally, the thickening degree type is classified into Concentrated (thickest at the innermost struts), Gradient (gradually thinner outward), and Spread (thinnest at the outermost struts). These are shown in Table 3, and all structures are classified into a total of 9 methods. For example, if the thickening shape type is 'Plus-type' and the thickening degree type is 'Concentrated', it is called 'Plus-concentrated'. In the case of the Gradient-Type structure, the mass of the cells in Area 1 and Area 3 is designed to have the same difference from the mass of the cells in Area 2, maintaining the total mass.



(**a**) Center-type (**b**) I-type (**c**) Plus-type

Figure 11. Shape types of adjusting internal method.

Table 3. Distributing strut radius types of adjusting internal method.

Type	Strut Radius
Concentrated	Area 1 > Area 2 = Area 3
Gradient	Area 1 > Area 2 > Area 3
Spread	Area 1 = Area 2 > Area 3

Since the mass of the 5 × 5 × 5 structure is designed the same, as the inner struts become thicker, the thickness of the outer struts becomes thinner. To quantify this, the standard deviation of the mass ratio of a total of 125-unit structure (12 mm × 12 mm × 12 mm) is calculated. The formula for calculating the standard deviation of the mass ratio is given by Equation (12) [32]. refers to the standard deviation of the mass ratio, X refers to the average value of a 125-unit structure mass ratio, x refers to a mass ratio of each unit structure. n refers to the number of unit cell structures.

$$s = \sqrt{\frac{\sum (X - x)^2}{n}} \tag{12}$$

A structure with a high mass ratio standard deviation means that the inner struts are relatively thicker, resulting in a structure with concentrated mass. Conversely, a structure with a low mass ratio standard deviation means that the inner struts are relatively thinner. When all the struts in the structure have the same thickness, the mass ratio standard deviation becomes '0'.

2.5. Finite Element Analysis

Before manufacturing the structure, a compression analysis on a 5 × 5 × 5 structure using FEA was conducted. To observe the energy-absorbing behavior of the structure composed of multiple elements, a quasi-static compression analysis is performed on the 5 × 5 × 5 structure with a 2-node linear beam in space (B31). Based on the mesh convergence study, the number of elements is determined. For the BCCz+cross 5 × 5 × 5 structure, it is composed of 10,210 nodes and 11,040 elements and analyzed using explicit finite element methods. Unlike the unit structures composed of 3D solid elements, 3D beam elements are used for computational efficiency in analysis time [33]. As shown in Figure 12, the boundary conditions and contact conditions of the analysis are the same as those for the unit structures, except for a compression speed of 60 mm/s. Also, the mesh conditions of the BCCz+cross 5 × 5 × 5 structure are illustrated in Figure 12.

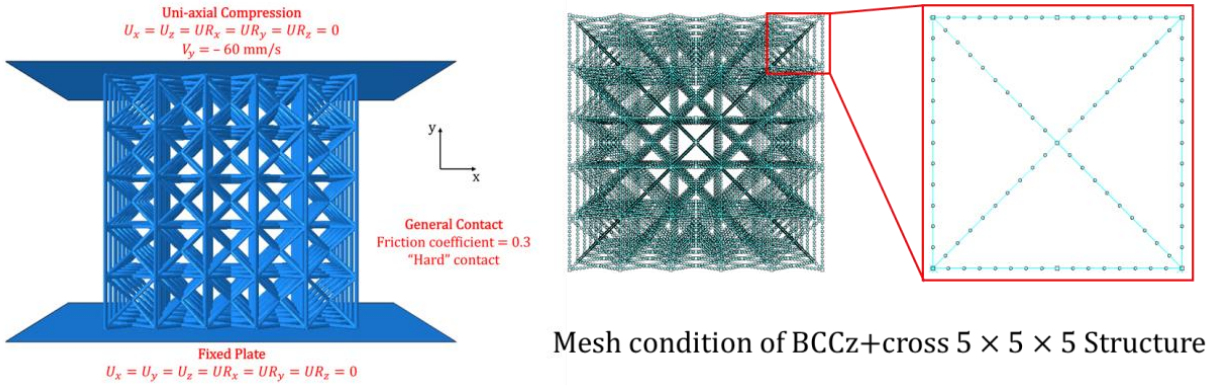


Figure 12. Finite element analysis conditions for BCCz+cross 5 × 5 × 5 structure in compression test.

2.6. Design of Experiments

2.6.1. Creation of Surrogate Model

A surrogate model, also known as a metamodel, is an engineering method for creating a mathematical model that represents the relationship between design variables and response functions. Methods such as FEA can be utilized in the design process to determine the system response. However, as systems become more complex, their application in the design process becomes increasingly time-consuming and expensive. To address these challenges, an approximation-based data model is constructed. This model is referred to as a surrogate model. The process of creating these surrogate models is also called metamodeling. This involves extracting samples through the DoE (Design of Experiment) and constructing the surrogate model through the estimation of the sample data.

In this study, the surrogate model is developed to obtain the *MCF* in terms of the total mass and the mass ratio standard deviation of lattice structures. Once the mass ratio distribution of each cell is established, the standard deviation of the mass ratio can be derived. Conversely, once the standard deviation of the mass ratio is known, the corresponding mass ratio distribution for each cell can be determined, owing to the advantages of the previously described group-wise density control scheme. Therefore, through the constructed surrogate model, one can obtain the group-wise density-adjusted energy-absorbing structure with the desired performance.

2.6.2. Compensated Latin Hypercube Sampling Method

Unlike physical experiments, computational analysis does not require repeated analysis, as there are no errors arising from input values. However, a large number of analysis data points are required to construct a more accurate surrogate model. In the classical FFD (Full-Factorial Design) method, the number of sample points required depends on the levels of input data and the number of factors, requiring $(levels)^n$ sample points. If the analysis plan is constructed using classical sampling methods like FFD, accurate data can be obtained, but the time cost increases exponentially with the number of sample points, making it inefficient for constructing a surrogate model plan. Therefore, in this study, an efficient analysis plan is constructed using the LHS (Latin Hypercube Sampling) method [34]. LHS is an experiment planning method that selects one sample point at each level for two input variables, as shown in Figure 13. This method prevents sample points from overlapping and allows for uniformly distributed sample points, enabling efficient analysis of the variable space at minimal cost. However, for complex systems with many design variables, errors tend to increase near the boundaries if the levels are set too low. To reduce this error, 20 sample points using LHS and an additional 15 boundary points are selected, resulting in a total of 35 sample points. The plan is based on the structure's mass and the mass ratio's standard deviation as input variables.

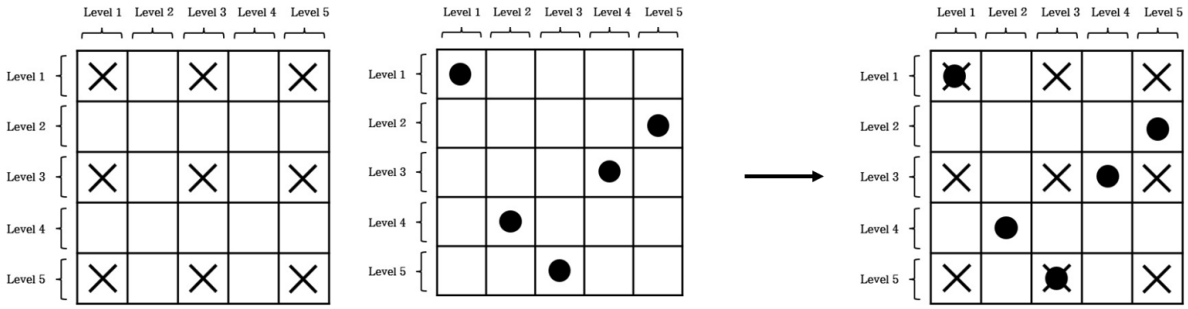


Figure 13. Illustration of compensated Latin hypercube sampling.

In this study, the mass of the structures is determined uniformly, with strut radius ranging from 0.5 mm to 0.75 mm. The reason for setting the range of the strut radius is that the energy-absorbing structure is designed to be applied to AAM, and it has sufficient *MCF* performance within the radius range of 0.5 mm to 0.75 mm. Therefore, one input variable, mass, ranges from approximately 50.29 g for a $5 \times 5 \times 5$ structure with a 0.5 mm strut radius to approximately 107.48 g for a $5 \times 5 \times 5$ structure with a 0.75 mm strut radius. Another input variable, the standard deviation of the mass ratio, is determined based on the minimum radius of 0.3 mm, manufacturable by EBM, and the maximum radius of 1.5 mm, where initial densification due to contact does not occur during compression, allowing energy absorption through deformation.

Table 4 illustrates an example of determining manufacturability using a Center-Gradient type structure with a mass of 76.59 g. As it moved from No. 1 to No. 4, the standard deviation of the mass ratio increased. In the case of No. 4, the strut radius is less than the minimum radius of 0.3 mm and exceeds the maximum design radius of 1.5 mm to minimize contact effects. Therefore, No. 4 is considered an unmanufacturable model. This method identifies manufacturable models for a total of 9 internal density-adjusted types. These data show that compensated LHS is conducted to determine only sample points for manufacturable models.

Table 4. Example of determining the manufacturability of an energy-absorbing structure.

No.	Radius [mm]	Mass [g]	Mass Ratio STD [%]	Manufacturability
1	0.625/0.625/0.625	76.59	0	Acceptable
2	0.4/0.8604/1.3208	76.59	6.78	Acceptable
3	0.34/0.8996/1.4592	76.59	8.23	Acceptable
4	0.25/0.9440/1.6380	76.59	10.06	Unacceptable

2.6.3. Universal Kriging Interpolation

It is necessary to determine an appropriate method to construct a surrogate model using the sample points set through the analysis plan. This study uses interpolation to build a response surface and predict unknown values using the sample points. Interpolation is a method of estimating unknown values based on known data points. In this study, 3D spatial interpolation (GIS, Geographic Information System interpolation) is used to obtain one response variable from two input variables.

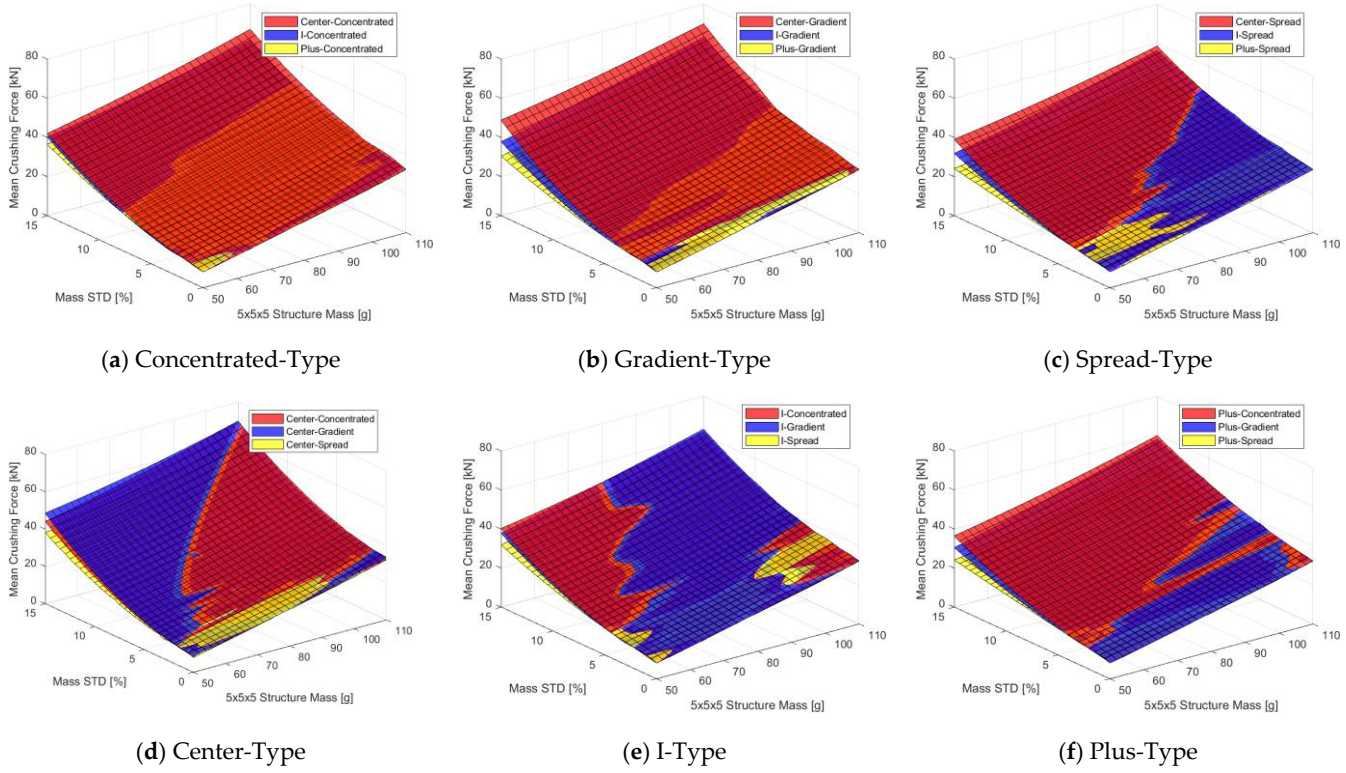
Spatial interpolation methods can be broadly divided into IDW (Inverse Distance Weighted), which determines new cell values using linearly combined weights from nearby points; Kriging Interpolation, a geostatistical method that predicts attribute values at points of interest using a linear combination of known data; and Spline Interpolation, which generates curves that connect each point. Among these, Kriging Interpolation is adopted

in this study, as it can accurately predict values by considering the correlation strength between neighboring values as well as the distance from measured values [35].

Using values extracted through Kriging Interpolation, a response surface is constructed, and the energy-absorbing structure is designed to meet the desired performance based on the response surface. Kriging Interpolation follows Equation (13). x_0 is a target point and ${Z_\omega}^*(x_0)$ refers to the universal kriging predictor of the value of random function $Z(x)$ and ω_i refers to weight, a_l refers to unknown coefficients, f_l refers to deterministic functions of the geographical coordinates. $Y(x_i)$ refers to a real-valued residual random function.

$$ {Z_\omega}^*(x_0) = \sum_{i=0}^{n} \omega_i \left(\sum_{l=0}^{L} a_l f_l(x) + Y(x_i) \right) = \boldsymbol{\omega}^T (\mathbf{Fa} + \mathbf{Y}) \tag{13} $$

The constructed response surfaces using Kriging Interpolation are shown in Figure 14. Response surfaces are constructed for nine different methods of adjusting internal density, with the mass of the structure and the standard deviation of the mass ratio as the two input variables. The response variable obtained is the *MCF* of the structures. Depending on the method of adjusting internal density, there are cases where the structure cannot be manufactured, resulting in different maximum values of the mass ratio standard deviation. Therefore, it is necessary to refer to the design data for manufacturability.



(**a**) Concentrated-Type (**b**) Gradient-Type (**c**) Spread-Type

(**d**) Center-Type (**e**) I-Type (**f**) Plus-Type

Figure 14. Comparison of response surfaces constructed using universal kriging interpolation.

The constructed response surface can be used to obtain design data for extracting structures with the desired performance through one-to-one correspondence. It is confirmed that the structures with the same mass can have improved energy-absorbing performance depending on the type of adjusting internal density. Regardless of the type used to adjust internal density, it is observed that the energy absorption performance improves as the mass and standard deviation of the mass ratio increases.

According to Figure 14a–c, Center-Type, I-Type, and Plus-Type structures show the higher *MCF* performance in that order. This indicates that the *MCF* performance improves when the thickness of the structure is concentrated in a smaller number of struts. However, if reinforcement is concentrated on a small number of struts, the global buckling may occur when subjected to vertical loads, preventing proper energy absorption.

Also, in Figure 14d,e, it can be observed that the Gradient-Type structures seem to have similar *MCF* performance to the Center-Type and I-Type structures, while the Spread-Type structure appears to have lower *MCF* performance compared to other types. Additionally, it can be observed that Concentrated-Type, Gradient-Type, and Spread-Type structures show higher *MCF* performance in that order in Figure 14f.

As a result, it is confirmed that the Center-Type structures have the highest *MCF* performance, and the Concentrated-Type and Gradient-Type structures have similar performance. Therefore, the Center-Concentrated and Center-Gradient structures are manufactured using metal 3D additive manufacturing technology, and their energy-absorbing performance is verified.

3. Experiments

3.1. Metal Additive Manufacturing Method

Data points within the response surface are extracted to verify the constructed response surface, and energy-absorbing structures are manufactured and subjected to compression tests. This study uses a metal additive manufacturing technique, specifically the EBM method. This method involves sintering metal powder by irradiating it with an electron beam and then stacking the sintered layers. Compared to the SLS (Selective Laser Sintering) method used in many studies for lattice structures, EBM has the advantage of being produced in a vacuum, resulting in lower residual stress in the structures and reduced concerns about hydrogen embrittlement that can degrade the physical properties of the product. Additionally, manufacturing at a high temperature of approximately 700 °C reduces warping in the product. In metal additive manufacturing, supports are needed depending on the gap between the outputs and the stacking angle of the output [36]. In the case of EBM, fine powder acts as a support between the outputs, making removal support easier. Although the surface finish is not great, this does not significantly affect the crashworthiness of the structure, making it an optimized metal additive manufacturing technique for this study. Based on the results of the constructed response surface, one Center-Concentrated structure and two Center-Gradient structures are adopted to be manufactured. Additionally, a uniform structure is also manufactured for comparison. The designed models and manufactured models are shown in Figure 15. The Uni. refers to uniform, and it is the meaning of the structure that has the same strut radius. C-Con. refers to Center-Concentrated and C-Gra. refers to Center-Gradient. The differences in the strut radius for each area of the structures have been depicted using colored bar graphs for easier to compare the area of the structure and the strut radius of the structure.

The structures are manufactured using GE Additive's Arcam EBM Spectra H Machine, and the metal powder used is Ti-6Al-4V Grade 5, with an average particle size of 45–106 μm. The electron beam power used for the build ranged from 900 W to 1800 W, with a scan speed of 4530 mm/s. The sintered powder is stacked with a layer thickness of 50 μm.

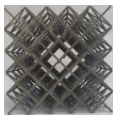
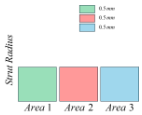
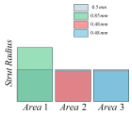
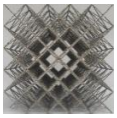
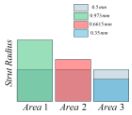
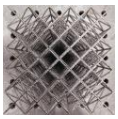
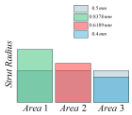
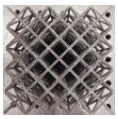
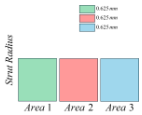
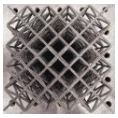
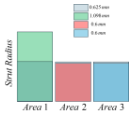
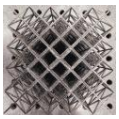
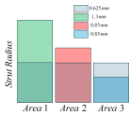
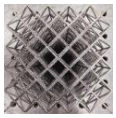
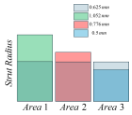
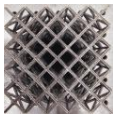
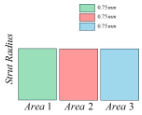
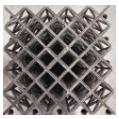
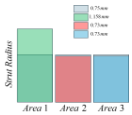
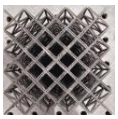
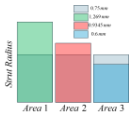
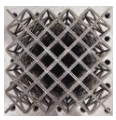
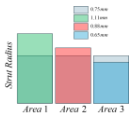
Model	Type	Designed Mass [g]	Standard Deviation of Mass Ratio [%]	Configuration (FEM Designed)	Configuration (EBM Manufactured)	Strut Radius Comparison
Model 1–1	Uni.	50.29	0			
Model 1–2	C-Con.	50.29	1.92			
Model 1–3	C-Gra.	50.29	3.62			
Model 1–4	C-Gra.	50.29	2.67			
Model 2–1	Uni.	76.59	0			
Model 2–2	C-Con.	76.59	2.88			
Model 2–3	C-Gra.	76.59	6.79			
Model 2–4	C-Gra.	76.59	4.00			
Model 3–1	Uni.	107.48	0			
Model 3–2	C-Con.	107.48	2.65			
Model 3–3	C-Gra.	107.48	5.51			
Model 3–4	C-Gra.	107.48	3.75			

Figure 15. Configuration of EBM-manufactured models and design variables (top view).

3.2. Quasi-Static Compression Test

To verify the energy-absorbing performance of the manufactured structures, a quasi-static compression test is conducted. During this test, the force applied to the load cell of the UTM is measured according to the compressive displacement to determine the compressive force of the structure. A comparison between the experimental data and the

FEA data is conducted. The UTM used for the quasi-static compression tests in this study is SHIMADZU's AG-X Plus 300 kN, and the compression speed is set to 10 mm/min with displacement control. A total of 12 fabricated structures are tested under identical ambient temperature conditions without any additional post-processing. The entire testing process, including specimen deformation, is documented through photographs and videos. In Figure 16, the compressive behavior of the Model 1–1 structure is presented, corresponding to the compressive displacement during the compression test. The lattice structure is captured at a 45-degree angle to display its x and y-axis configurations. Diagonal failure is observed during compression, and the compressive failure mechanisms obtained from FEA are found to closely match the experimental results. For a physical interpretation of the failure mechanism, a previous study can be referred to [13].

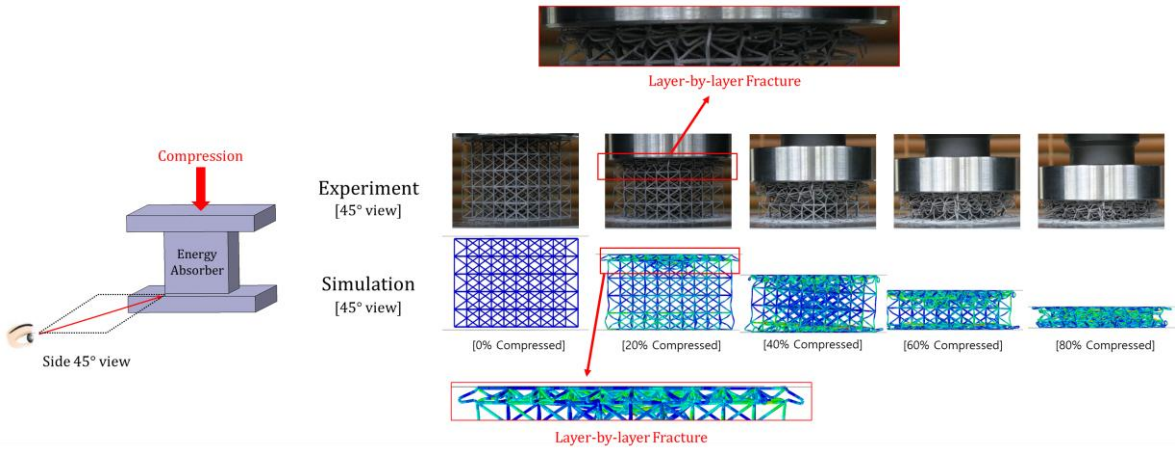


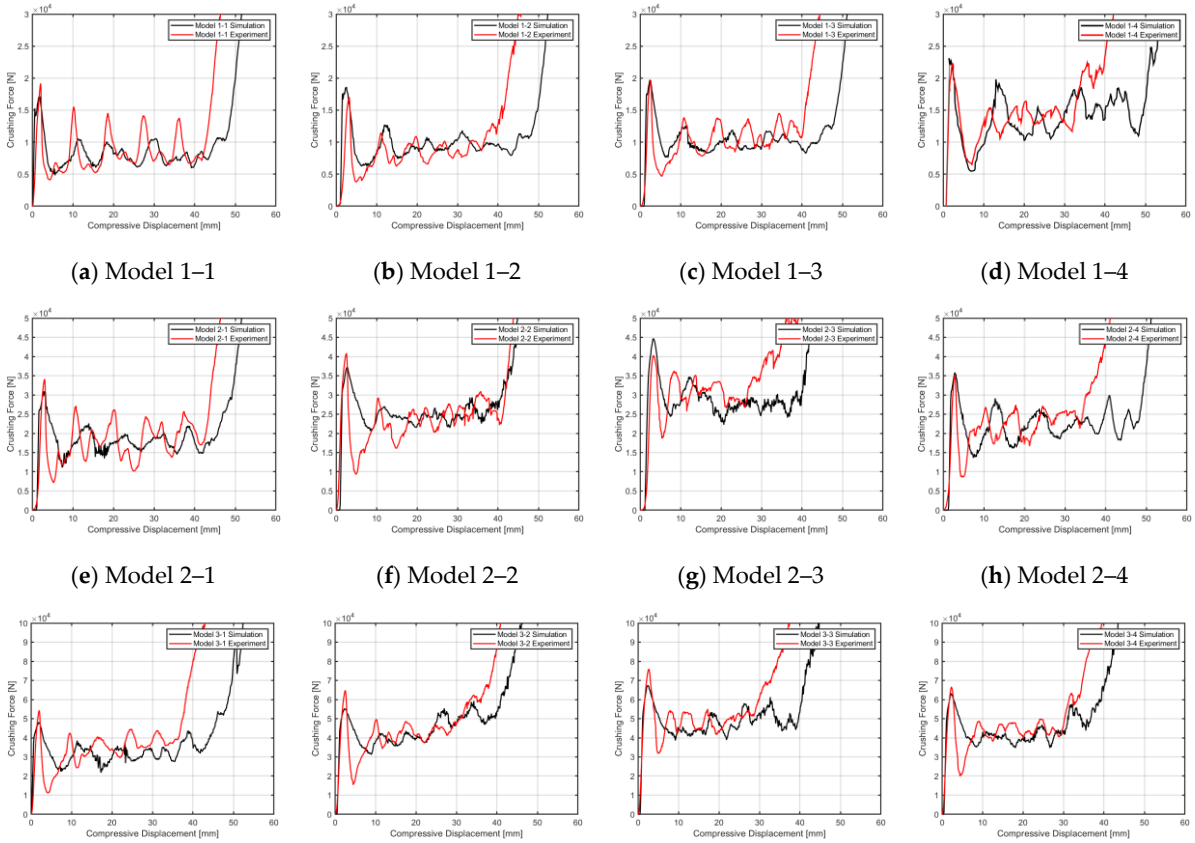
Figure 16. Compression test on energy-absorbing structure (Model 1–1) by UTM (Side 45° view).

3.3. Results and Discussion

The compressive force data obtained by the compression test are then compared with the FEA data, as shown in Figure 17. By comparing Figure 17a–l, it is confirmed that the compressive force curve between the FEA and the experiment of the energy-absorbing structure is within a similar force range. However, it is observed that after reaching the initial peak crushing force during the compression of the energy-absorbing structure manufactured using the EBM method, the compressive force decreased rapidly. This is due to the brittleness of the Ti-6Al-4V material [37], which is printed with a thin thickness. Additionally, it is noted that the compressive displacement of the energy-absorbing structures manufactured using the EBM method is generally shorter. This is attributed to the inability to accurately implement the contact conditions of the actual thickness in the simplified design using B31 elements in FEA. Nevertheless, since compressive displacement does not significantly affect *MCF*, the data error is considered to be minimal.

The compressive analysis and experimental data of the energy-absorbing structure are quantitatively compared, as shown in Tables 5–7. M.STD refers to the standard deviation of the mass ratio, *S.MCF* refers to simulated *MCF* and it is the *MCF* calculated by FEA. And *E.MCF* refers to an experiment *MCF* and it is the *MCF* calculated from the data from the quasi-compression test. The experimental data verified that adjusting the internal density of the lattice structure can improve the energy absorption performance, as indicated by the response surface results. Additionally, when comparing Model 1–3 and Model 1–4, as well as Model 2–3 and Model 2–4, Model 3–3 and Model 3–4, it is confirmed that the energy- absorbing performance improved as the standard deviation of the mass ratio of the structure increased. However, there is an error between the experimental and analytical results shown in the *MCF*. The reason for the discrepancy is not considered

to account for the contact effect between the thickness of struts and the brittleness of the Ti-6Al-4V material.



(**a**) Model 1–1 (**b**) Model 1–2 (**c**) Model 1–3 (**d**) Model 1–4

(**e**) Model 2–1 (**f**) Model 2–2 (**g**) Model 2–3 (**h**) Model 2–4

(**i**) Model 3–1 (**j**) Model 3–2 (**k**) Model 3–3 (**l**) Model 3–4

Figure 17. Comparison of displacement–force curve for energy absorbers between experiment and analysis.

Table 5. Quantitative comparison of *MCF* data for energy-absorbing structures with a designed mass of 50.24 g.

Model	**Model 1–1**	**Model 1–2**	**Model 1–3**	**Model 1–4**
Type	Uni.	C-Con	C-Gra.	C-Gra.
M.STD [%]	0	1.92	3.62	2.67
S.MCF [N]	8.17×10^3	9.51×10^3	1.20×10^4	1.04×10^4
E.MCF [N]	8.27×10^3	8.44×10^3	1.30×10^4	1.01×10^4
Error [%]	1.2	−11.2	8.3	−2.9

Table 6. Quantitative comparison of *MCF* data for energy-absorbing structures with a designed mass of 76.59 g.

Model	**Model 2–1**	**Model 2–2**	**Model 2–3**	**Model 2–4**
Type	Uni.	C-Con.	C-Gra.	C-Gra.
M.STD [%]	0	2.88	6.79	4.00
S.MCF [N]	1.85×10^4	2.52×10^4	2.87×10^4	2.20×10^4
E.MCF [N]	1.75×10^4	2.31×10^4	3.03×10^4	2.15×10^4
Error [%]	−5.4	−7.9	5.5	−2.3

Table 7. Quantitative comparison of *MCF* data for energy-absorbing structures with a designed mass of 107.48 g.

Model	Model 3–1	Model 3–2	Model 3–3	Model 3–4
Type	Uni.	C-Con	C-Gra.	C-Gra.
M.STD [%]	0	2.65	5.51	3.75
S.MCF [N]	3.10×10^4	4.38×10^4	4.78×10^4	4.40×10^4
E.MCF [N]	3.33×10^4	4.26×10^4	5.01×10^4	4.32×10^4
Error [%]	7.4	−2.7	4.8	−1.8

4. Vertical Drop Collision Simulation

It is confirmed that adjusting the internal density allows for the design of energy-absorbing structures with various energy-absorbing performance characteristics in the same mass condition. The lattice-based energy-absorbing structure is adopted for application in AAM using the constructed response surface, and a crash simulation of the vertical drop test was conducted to verify it. The crash simulation is performed using the same finite element commercial software, ABAQUS, used for quasi-static compression analysis, and an explicit analysis was conducted. As shown in Figure 18, the structure is placed at a height of 420 mm between two rigid plates, and a point mass is assigned to the upper plate. A vertical crash velocity of 10 m/s is assigned as the initial condition. The lower plate is fixed, and gravitational acceleration of 9.8 m/s^2 is applied in the direction of the vertical drop. This analysis aimed to verify the design of the energy-absorbing structure through equations by confirming that the acceleration transmitted to the upper plate is below the human tolerance (25.9 G).

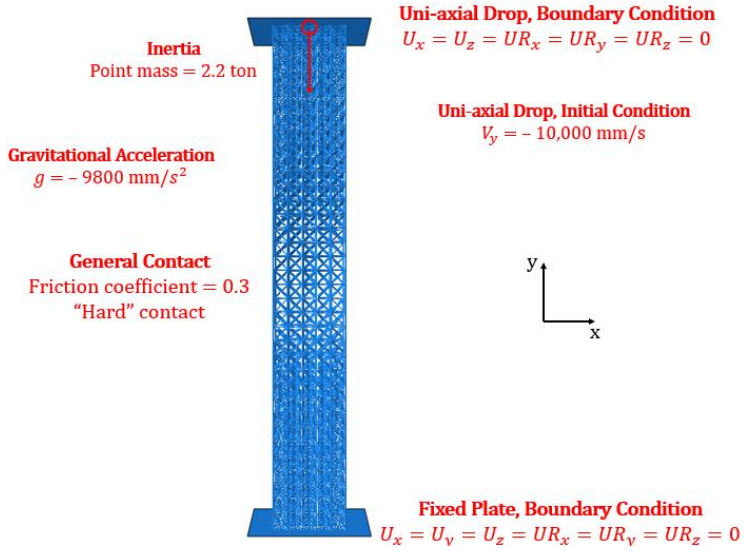


Figure 18. Finite element analysis setting conditions for the crash simulation of the vertical drop test.

The gross weight is assumed to be 2200 kg for the AAM model, with a compressive displacement of 300 mm. The survivable acceleration limit $a_{\max}$ is adopted as 20 G. Using the values of variables and Equation (8), the *MCF* range of the energy-absorbing structure for the AAM model can be calculated as $388,227\ \text{N} \leq \text{F} \leq 452,760\ \text{N}$. Assuming the energy-absorbing structure, with an area of 300 mm × 300 mm, is installed on the subfloor of the 2200 kg AAM model, the required *MCF* value for the 5 × 5 × 5 lattice structure with 12 mm cube cells, having an area of 60 mm × 60 mm, corresponds to 1/25 of the required

range ($388,227\ \text{N} \leq \text{F} \leq 452,760\ \text{N}$) for the entire energy-absorbing structure of the AAM model, as given by Equation (14).

$$15,529\ \text{N} \leq \text{F} \leq 18,110\ \text{N} \tag{14}$$

A structure with *MCF* of 16,819 N, which is the average value of high-limitation and low-limitation crushing force within the range, is selected as shown in Figure 19. The structure within is required *MCF* range is a $5 \times 5 \times 5$ structure with a mass of 0.054 kg and a mass ratio standard deviation of 6.01% using the Center-Gradient method. In contrast, a Uniform structure with the same *MCF* performance has a mass of 0.078 kg, showing an increase in mass of approximately 44%. The reinforced structure using the Center-Gradient method is subjected to vertical drop collision analysis to calculate the acceleration transmitted to the upper plate and verify its energy-absorbing performance.

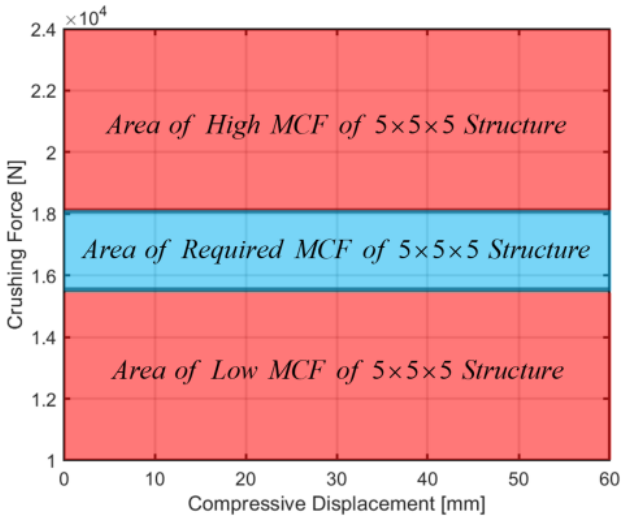
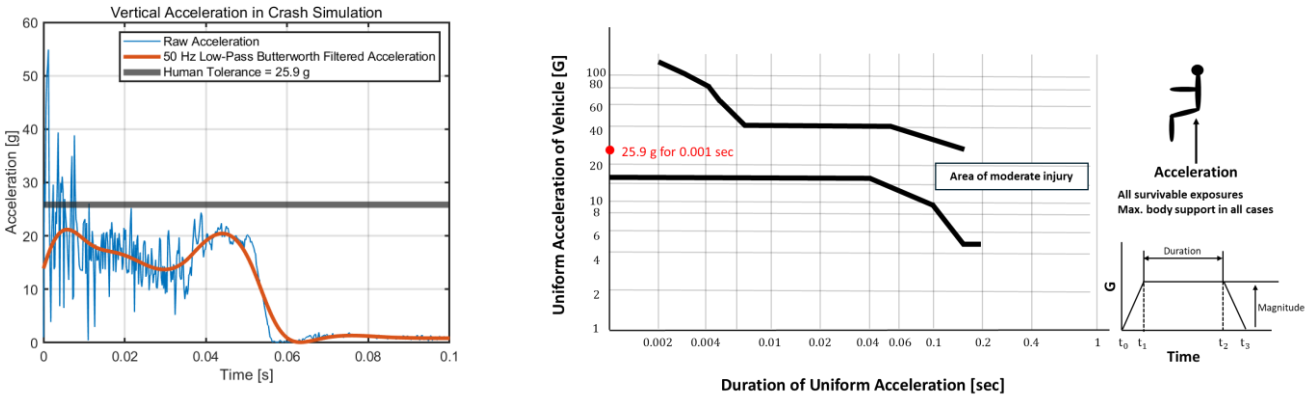


Figure 19. Area of required *MCF* of $5 \times 5 \times 5$ structure for 2200 kg AAM.

Fasanella et al. described procedures, data processing techniques, and practical ideas for modeling aircraft crash analysis and recommended the following for aircraft structural crash test and analysis data processing techniques. In a typical survivable crash, seated passengers are not affected by high-frequency acceleration signals. To extract the main crash acceleration that affects them, a low-pass filter should be applied. Applying near 50 Hz low-pass filter has produced good results [38]. In the literature [39], a cutoff frequency range of 20 Hz to 80 Hz is suggested. Therefore, in this study, the average of the minimum and maximum suggested values of 50 Hz is adopted. The acceleration graph obtained through the crash simulation of the vertical drop test is shown in Figure 20a. In this study, a low-pass Butterworth filter is used to extract the main acceleration [40].

Through the low-pass Butterworth filter, it is confirmed that the main acceleration transmitted to the upper plate during the impact absorption process is around 20 G, which did not exceed the vertical human tolerance load of 25.9 G. On the other hand, very short peaks of acceleration over 25.9 G are also observed in the raw data, although their durations are too short to cause fatal harm to the human body. The corresponding duration is approximately 0.001 s, which falls within the moderate injury region of the Eiband curve as shown in Figure 20b. Additionally, from a numerical point of view, high-frequency numerical noise may be included because damping is not applied in numerical simulation, unlike in real-world situations. To enhance passenger safety to a higher standard, alleviation of such brief peak accelerations could be considered as a next step for future work.



(**a**) (**b**)

Figure 20. Low-pass Butterworth filtered acceleration of crash simulation of vertical drop test. (**a**) Low-pass Butterworth filtered acceleration. (**b**) Point plot of accelerations exceeding 25.9 G and its duration based on Figure 20a raw acceleration data.

5. Conclusions

In this study, the requirement for *MCF*, that energy-absorbing structures should satisfy during emergency landings is derived in terms of the mass of the AAM, the landing velocity, and the crushable length of the energy-absorbing structures. From the requirement, it is known that the mean crushing force should be in a certain range to prevent transferring excessive acceleration to the human body. After derivation, a group-wise density control scheme is newly proposed to enhance the energy absorption capability while maintaining the total mass of the lattice structure, and a surrogate model for *MCF* is constructed in terms of total mass and the standard deviation of mass ratio, along with the proposed density control scheme. Through the constructed surrogate model, the group-wise density-adjusted energy-absorbing structure can be obtained, which satisfies the design requirement for *MCF*.

The internal density-adjusted types are classified as Center-Type, I-Type, and Plus-Type, and these are further divided into Concentrated-Type, Gradient-Type, and Spread-Type, resulting in nine response surfaces. Compensated LHS is used to construct the nine response surfaces, with a total of 35 sample points. The findings from the response surfaces are as follows:

1. Structures with adjusted internal density show improved performance of energy absorption compared to structures with uniform strut thickness.
2. Regardless of the internal density-adjusted type, increasing the standard deviation of the mass ratio by concentrating the strut thickness in specific areas led to improved *MCF*.
3. The Concentrated- and Gradient-Types, which excessively concentrate on specific areas, exhibited similar performance, while the Spread method showed slightly lower improvements in energy absorption performance. Compared to the Concentrated-Type, the Gradient-Type is expected to allow more stable energy absorption as it distributes the strut radius more widely, reducing the likelihood of global buckling during compression.

To verify these findings, a quasi-static compression test is conducted on structures manufactured using the EBM additive manufacturing. Although it is observed that there are some differences compared to the tests due to difficulties in implementing brittleness and contact conditions in the FEA, it is also known that the overall trends still follow the expected pattern. Finally, to design the energy-absorbing structure for AAM, a crash

analysis of the vertical drop test is conducted to calculate the acceleration transmitted to the upper structure. The result of the main acceleration extracted from a 50 Hz low-pass filter is under 25.9 G, which is within the human tolerance acceleration range. It verifies the energy absorption capability of the proposed lattice structure and the usefulness of the proposed design procedure. On the other hand, a very short peak of acceleration exceeding 25.9 G lasting around 0.001 s is observed in the raw data, although it does not cause fatal injury to the human body. Therefore, it is deemed necessary to alleviate such brief peak acceleration through further research efforts to enhance passenger safety to a higher standard.

Author Contributions: Conceptualization, J.C. and J.Y.C.; Methodology, J.C., J.H.K., C.-Y.L. and J.Y.C.; Software, J.C. and E.S.L.; Validation, J.C. and E.S.L.; Formal analysis, J.Y.C.; Investigation, J.C., E.S.L., J.H.K., C.-Y.L. and J.Y.C.; Resources, J.C. and E.S.L.; Data curation, J.C. and E.S.L.; Writing—original draft, J.C.; Writing—review and editing, E.S.L., J.H.K., C.-Y.L. and J.Y.C.; Visualization, J.C. and E.S.L.; Supervision, J.H.K., C.-Y.L. and J.Y.C.; Project administration, J.Y.C.; Funding acquisition, J.Y.C. All authors have read and agreed to the published version of the manuscript.

Funding: This study was supported by the National Research Foundation of Korea (NRF) grant funded by the Korean Government (MSIT) (No. 2021R1A5A1031868).

Institutional Review Board Statement: Not applicable.

Data Availability Statement: The original contributions presented in this study are included in the article; further inquiries can be directed to the corresponding authors.

Conflicts of Interest: The authors declare no conflicts of interest.

Abbreviations

The following abbreviations are used in this manuscript:

AAM	Advanced Air Mobility
BCC	Body-Centered Cubic
BCCz+cross	BCC with vertical and X-shaped cross-linked horizontal auxiliary struts
C-Con.	Center-Concentrated Type
C-Gra.	Center-Gradient Type
CAD	Computer-Aided Design
DoE	Design of Experiment
EA	Energy Absorption
EBM	Electron Beam Melting
E.MCF	*MCF* calculated by the data extracted from the quasi-compression test
eVTOL	electric Vertical Take-Off Landing
FEA	Finite Element Analysis
FEM	Finite Element Method
FAA	Federal Aviation Administration
FFD	Full-Factorial Design
IDW	Inverse Distance Weighted
ICAO	International Civil Aviation Organization
LHS	Latin-Hypercube Sampling
MCF	Mean Crushing Force
M.STD	Standard Deviation of Mass Ratio
NASA	National Aeronautics and Space Administration
SLS	Selective Laser Sintering
STD	Standard Deviation
S.MCF	*MCF* calculated by FEA
Uni.	Uniform Type
UTM	Universal Test Machine

References

1. Guo, J.; Chen, L.; Li, L.; Na, X.; Vlacic, L.; Wang, F.-Y. Advanced Air Mobility: An Innovation for Future Diversified Transportation and Society. *IEEE Trans. Intell. Veh.* **2024**, *9*, 3106–3110. [CrossRef]
2. Bridgelall, R. Aircraft Innovation Trends Enabling Advanced Air Mobility. *Inventions* **2024**, *9*, 84. [CrossRef]
3. Ellis, K.; Koelling, J.; Davies, M.; Krois, P. *In-Time System-Wide Safety Assurance (ISSA) Concept of Operations and Design Considerations for Urban Air Mobility (UAM)*; NASA Technical Report; NASA Langley Research Center: Hampton, VA, USA, 2020.
4. Laarmann, L.; Thoma, A.; Misch, P.; Koppel, T.; Schumann, H.; Hornung, M. Automotive Safety Approach for Future eVTOL Vehicles. *CEAS Aeronaut. J.* **2023**, *14*, 369–379. [CrossRef]
5. U.S. Army Research and Technology Laboratories (AVRADCOM). *Aircraft Crash Survival Design Guide*; Report No. USARTL-TR-79-22A; U.S. Army Research and Technology Laboratories: Fort Eustis, VA, USA, 1979.
6. U.S. Army Research and Technology Laboratories (AVRADCOM). *Aircraft Crash Survival Design Guide*; Report No. USARTL-TR-79-22B; U.S. Army Research and Technology Laboratories: Fort Eustis, VA, USA, 1979.
7. U.S. Department of Defense. *Military Standard: Aircraft Crash Survival Design Guide*; MIL-STD-1290A; U.S. Department of Defense: Washington, DC, USA, 1989.
8. Federal Aviation Administration. *Federal Aviation Regulations: Emergency Landing Dynamic Conditions*; FAR Part 23.562; Federal Aviation Administration: Washington, DC, USA, 2011.
9. Federal Aviation Administration. *Federal Aviation Regulations: Emergency Landing Dynamic Conditions*; FAR Part 27.562; Federal Aviation Administration: Washington, DC, USA, 2024.
10. Bai, Y.; Xiong, J.; Jin, L.; Tian, Q. Sandwich Structures for Energy Absorption Applications: A Review. *Materials* **2021**, *14*, 4731. [CrossRef]
11. Yin, X.; Jiang, Y.; Huang, Z.; Guo, X.; Zhao, Y.; Feng, Y. Research on a Honeycomb Structure for Pyroshock Isolation at the Spacecraft–Rocket Interface. *Aerospace* **2024**, *11*, 756. [CrossRef]
12. Schaedler, T.A.; Jacobsen, A.J.; Torrents, A.; Sorensen, A.E.; Lian, J.; Greer, J.R.; Valdevit, L.; Carter, W.B. Ultralight Metallic Microlattices. *Science* **2023**, *334*, 123–135. [CrossRef]
13. Cho, J.; Kim, E.; Kim, J.H.; Lee, C.-Y.; Cho, J.Y. Enhancement of Energy Absorption Capability of 3D Printed Ti-6Al-4V BCC Lattice Structures by Adding Auxiliary Struts. *Materials* **2025**, *18*, 732. [CrossRef]
14. Maskery, I.; Hussey, A.; Panesar, A.; Aremu, A.; Tuck, C.; Ashcroft, I.; Hague, R. An Investigation into Reinforced and Functionally Graded Lattice Structures. *J. Cell. Plast.* **2017**, *53*, 151–165. [CrossRef]
15. Mostafa, K.; Momesso, G.; Li, X.; Nobes, D.; Qureshi, A.J. Dual Graded Lattice Structures: Generation Framework and Mechanical Properties Characterization. *Polymers* **2021**, *13*, 2204. [CrossRef]
16. Sanchaniya, J.V.; Lasenko, I.; Gobins, V.; Kobeissi, A.; Goljandin, D. A Finite Element Method for Determining the Mechanical Properties of Electrospun Nanofibrous Mats. *Polymers* **2024**, *16*, 852. [CrossRef]
17. Duddeck, F.; Zimmer, H. Metamodel-Based Design Optimization–A Multidisciplinary Approach for Automotive Structures. In Proceedings of the FISITA 2012 World Automotive Congress, Beijing, China, 27–30 November 2012; Springer: Berlin/Heidelberg, Germany, 2013; pp. 1225–1237.
18. Box, G.E.P.; Wilson, K.B. On the Experimental Attainment of Optimum Conditions. *J. R. Stat. Soc. Ser. B* **1951**, *13*, 1–38. [CrossRef]
19. Czado, C.; Schepsmeier, U.; Lichtenstern, A. *Kriging Methods in Spatial Statistics*; Technical University of Munich: Munich, Germany, 2013.
20. Zhang, L.C.; Liu, Y.; Li, S.; Hao, Y. Additive Manufacturing of Titanium Alloys by Electron Beam Melting: A Review. *Adv. Eng. Mater.* **2018**, *20*, 1700842. [CrossRef]
21. Gibson, L.J.; Ashby, M.F. *Cellular Solids: Structure and Properties*; Cambridge University Press: Cambridge, UK, 1997.
22. Society of Automotive Engineers. *Performance Standard for Seats in Civil Rotorcraft, Transport Aircraft, and General Aviation Aircraft*; SAE AS8049 Rev B; SAE International: Warrendale, PA, USA, 2005.
23. Littell, J.; Putnam, J.; Annett, M.; Bark, L.; Jackson, K.; Fasanella, E. *A Summary of Test Results from a NASA Lift + Cruise eVTOL Crash Test*; NASA Technical Memorandum; NASA Langley Research Center: Hampton, VA, USA, 2023.
24. Eiband, A.M. *Human Tolerance to Rapidly Applied Accelerations: A Summary of the Literature*; NASA Memorandum 5-19-59E; National Aeronautics and Space Administration: Washington, DC, USA, 1959.
25. Kokil-Shah, S.; Sur, A.; Darvekar, S.; Shah, M. Recent Advancements of Micro-Lattice Structures: Applications, Manufacturing Methods, Mechanical Properties, Topologies and Challenges. *Arab. J. Sci. Eng.* **2021**, *46*, 204–220. [CrossRef]
26. Kamaraj, L.; Sudhan, P.H.S.; Bright, R.; Kannan, S.; Khalkar, V.; Sundaraiah, N. Quasi-static Compression Behavior and Crashworthiness of GLARE Laminate Conical Frustum with Progressive Circular and Square Cut-outs. *Polym. Compos.* **2023**, *44*, 3685–3697. [CrossRef]
27. Tao, C.; Wang, Z.; Liu, Z.; Wang, Y.; Zhou, X.; Liang, X.; Li, H. Crashworthiness of Additively Manufactured Lattice Reinforced Thin-Walled Tube Hybrid Structures. *Aerospace* **2023**, *10*, 524. [CrossRef]
28. Jerath, S. *Structural Stability Theory and Practice: Buckling of Columns, Beams, Plates, and Shells*; Wiley: Hoboken, NJ, USA, 2020.

29. Xu, Y. Research on Interpolation and Data Fitting: Basis and Applications. *arXiv* **2022**, arXiv:2208.11825.
30. Alwattar, T.; Mian, A. Development of an Elastic Material Model for BCC Lattice Cell Structures Using Finite Element Analysis and Neural Networks Approaches. *J. Compos. Sci.* **2019**, *3*, 33. [CrossRef]
31. Ghoddousi, S.; Mohammadnejad, M.; Safarabadi, M.; Haghighi-Yazdi, M. Compression Response of Nature-Inspired Metamaterials Based on Fibonacci Spiral. *Int. J. Mech. Sci.* **2025**, *285*, 109853. [CrossRef]
32. Airy, G.B. *On the Algebraical and Numerical Theory of Errors of Observations and the Combination of Observations*; Macmillan and Co.: London, UK, 1861.
33. Lei, H.; Li, C.; Meng, J.; Zhou, H.; Liu, Y.; Zhang, X.; Wang, P.; Fang, D. Evaluation of compressive properties of SLM-fabricated multi-layer lattice structures by experimental test and μ-CT-based finite element analysis. *Mater. Des.* **2019**, *169*, 107685. [CrossRef]
34. Tang, B. Orthogonal Array-Based Latin Hypercubes. *J. Am. Stat. Assoc.* **1993**, *88*, 1392–1397. [CrossRef]
35. Sagar, B.S.D.; Cheng, Q.; Agterberg, F. (Eds.) *Handbook of Mathematical Geosciences: Fifty Years of IAMG*; Springer: Cham, Switzerland, 2018; ISBN 978-3-319-78999-6.
36. Navi, N.U.; Tenenbaum, J.; Sabatani, E.; Kimmel, G.; David, R.B.; Rosen, B.A.; Barkay, Z.; Ezersky, V.; Tiferet, E.; Ganor, Y.I.; et al. Hydrogen effects on electrochemically charged additive manufactured by electron beam melting (EBM) and wrought Ti–6Al–4V alloys. *Int. J. Hydrog. Energy* **2020**, *45*, 25523–25540. [CrossRef]
37. Zhang, H.; Lu, D.; Pei, Y.; Chen, T.; Zou, T.; Wang, T.; Wang, X.; Liu, Y.; Wang, Q. Tensile behavior, microstructural evolution, and deformation mechanisms of a high Nb-TiAl alloy additively manufactured by electron beam melting. *Mater. Des.* **2022**, *225*, 111503. [CrossRef]
38. Camacho-García, A.; Llinares, R.; Lucas-Cuevas, A.G.; Pérez-Soriano, P. Influence of Accelerometer Signal Filtering on Automatic Detection of Gait Impact Parameters. *Int. J. Adv. Digit. Signal Process.* **2016**, *3*, 19–22.
39. Fasanella, E.L.; Jackson, K.E. *Best Practices for Crash Modeling and Simulation*; NASA/TM—2002-211944; National Aeronautics and Space Administration: Washington, DC, USA, 2002.
40. Selesnick, I.W.; Burrus, C.S. Generalized Digital Butterworth Filter Design. *IEEE Trans. Signal Process.* **1998**, *46*, 1688–1694. [CrossRef]

Disclaimer/Publisher's Note: The statements, opinions and data contained in all publications are solely those of the individual author(s) and contributor(s) and not of MDPI and/or the editor(s). MDPI and/or the editor(s) disclaim responsibility for any injury to people or property resulting from any ideas, methods, instructions or products referred to in the content.